BIOMEDICAL ENGINEERING MSc PROGRAM
UNIVERSITY OF CRETE
TECHNICAL UNIVERSITY OF CRETE
FOUNDATION FOR RESEARCH AND TECHNOLOGY-HELLAS

Application Grade Thesis

Refracting eye models

Student's Name: Eleni Voulgari | Supervisor's Name: Dimitris Papazoglou

20/12/2022

Refracting Eye models, optical models of the human eye, an overview

Table of Contents

ABSTRACT

The optical modeling of the human eye and the correct prediction of optical performance is a significant issue for light engineering as well as vision research since it is necessary to comprehend how the vision process functions before developing and designing precise optical systems and instruments to use in everyday clinical practice. The Gullstrand's schematic eye model, which earned the Nobel Prize in 1911, was one of several optical eye models that had been proposed in literature. Today, after 100 years of scientific progress, the advancement of ray tracing techniques and optical simulation software enables scientists to more accurately quantitatively duplicate the optical system of the human eye. Previous eye models, however, were more narrowly focused on a few parameters, such as corneal data, accommodation data, or aging data, and they employed either individualized or average population data as well as monochromatic or polychromatic light. Thus, no eye model can be defined as a complete optical system. In order to comprehend the vision process and its applications in ophthalmology, medical technology, and light engineering, it may be helpful to construct a comprehensive and accurate eye model. This thesis reviews optical eye models and sheds light on the key information that will be needed to create a full eye model utilizing modern technologies.

Keywords: Human eye models, optical system, refracting eye models, optical models

ΠΕΡΙΛΗΨΗ

Η οπτική μοντελοποίηση του ανθρώπινου ματιού και η σωστή πρόβλεψη της οπτικής απόδοσης αποτελούν σημαντικό ζήτημα για τη μηχανική του φωτός, καθώς και για την ερευνητική διαδικασία της όρασης, αφού είναι απαραίτητο να κατανοήσουμε πώς λειτουργεί η διαδικασία όρασης προτού αναπτύξουμε και σχεδιάσουμε ακριβείς οπτικά συστήματα και μέσα που θα χρησιμοποιηθούν στην καθημερινή κλινική πρακτική. Το γραφικό μοντέλο ματιού του Gullstrand, το οποίο απέσπασε το Βραβείο Νόμπελ το 1911, ήταν ένα από τα πολλά οπτικά μοντέλα ματιού που είχαν προταθεί στη βιβλιογραφία. Σήμερα, μετά από 100 χρόνια επιστημονικής προόδου, η πρόοδος των τεχνικών ανίχνευσης ακτινών και των οπτικών προσομοιωτών επιτρέπει στους επιστήμονες να αναπαράγουν με ακρίβεια και ποσοτικά το οπτικό σύστημα του ανθρώπινου ματιού. Ωστόσο, τα προηγούμενα μοντέλα ματιού επικεντρωνόντουσαν περισσότερο σε λίγες παραμέτρους, όπως δεδομένα της κορνέας, δεδομένα συγκέντρωσης ή δεδομένα γήρανσης, και χρησιμοποιούσαν είτε εξατομικευμένα είτε μέσα πληθυσμού, καθώς και μονοχρωματικό ή πολυχρωματικό φως. Έτσι, κανένα μοντέλο ματιού δεν μπορεί να οριστεί ως ένα πλήρες οπτικό σύστημα. Για να κατανοήσουμε τη διαδικασία της όρασης και τις εφαρμογές της στην οφθαλμολογία, την ιατρική τεχνολογία και τη μηχανική του φωτός, μπορεί να βοηθήσει η κατασκευή ενός συνεκτικού και ακριβούς μοντέλου ματιού. Αυτή η διατριβή κάνει ανασκόπηση των οπτικών μοντέλων ματιού και γνωστοποιεί τις βασικές πληροφορίες που θα χρειαστούν για να δημιουργηθεί ένα πλήρες μοντέλο ματιού με τη χρήση σύγχρονων τεχνολογιών.

Λέξεις κλειδιά: Μοντέλα ανθρώπινων ματιών, οπτικό σύστημα, διαθλαστικά μοντέλα ματιών, οπτικά μοντέλα

1. Introduction

The cornea and the crystalline lens are the only two positive lenses that make up the human eye, which is a reliable and straightforward optical device. The visual process is started when these lenses transfer pictures of the outside world onto the retina. The human eye is far more straightforward than artificial optical systems, which frequently employ several lenses layers in order to enhance picture quality. It does, however, fit the needs of the visual system effectively. The eye must use transparent living tissue rather than glass in order to provide high-resolution pictures in a wide field of vision for objects positioned at various distances. These is a substantially demanding task. An important factor of the vision process is also that the vision will only be clear if the pictures created on the retina are clear enough is crucial. On the other hand, the visual system will not work correctly and vision will be poor if the retinal pictures are blurry. There are numerous retinal and brain pathologies that can impair vision even when a good retinal picture is created; therefore the inverse of the previous statement is not necessarily true (Artal et al., 2014).

It is not at all unexpected that the eye is the most crucial optical system for the majority of people. And as is sometimes the case with the most significant things, it is frequently both venerated and disregarded. The eye is frequently considered by optical scientists and engineers to be so straightforward and well known in comparison to artificial optical systems that it does not warrant much consideration (Atchison et al., 2016).

Authors have significantly leaned on optical models of the eye during their research in the field of vision science. They did this to provide a framework for describing optical phenomena in vision, to forecast how changes in ocular biometry would impact aberrations, and as a computational tool to investigate the visual restrictions brought on by the eye's optical system. The aim of this thesis is to provide the latest evidence derived from the latest scientific literature regarding the theoretical background of the refracting eye models that have been proposed (Atchison et al., 2016).

2. The optical instrument of the eye

An adult human's eye is roughly a spherical construct with a 24 mm diameter. Except for the anterior section, where the clear cornea enables the light to enter the eye, it is externally covered by a strong and flexible tissue called the sclera. The choroid, which supplies nutrients, and the retina, where light is absorbed by the photoreceptors following image generation, are two additional layers that are internal to the sclera. Six external muscles move the eye, allowing fixation and scanning of the surrounding visual field. The cornea, a thin transparent layer devoid of blood vessels with a central thickness of around 0.55 mm and a width of about 12 mm, is responsible for the initial refractive action of light entering the eye (Artal et al., 2014, LeGrand et al., 2013).

To provide the highest possible image quality, an aqueous tear film on the cornea ensures that the initial optical surface is smooth. The aqueous humor, which is a substance that resembles water, fills the anterior chamber next to the cornea. The iris functions as a diaphragm and consists of two sets of muscles with a central hole whose size is determined by the contraction of the muscles. The number and distribution of pigments in this section of the eye provide the iris's distinctive hue. The iris's central opening, known as the aperture, controls the quantity of light that enters the eye. The picture of the iris as seen through the cornea is defined as the entry pupil, while the image of the aperture as seen through the lens is defined as the exit pupil. From less than 2 mm in diameter in strong light to more than 8 mm in light absence, the aperture size varies accordingly to the ambient light (Woodman et al., 1996, LeGrand et al., 2013).

The pupil’s main role is the regulation of retinal illumination and the restriction of the amount of light that enters the eye, which has a direct impact on retinal picture quality. The crystalline lens joins with the cornea after the iris in order to create the pictures on the retina. The crystalline lens is an active optical component, whereas the cornea is a lens with standard optical power. Thus, the crystalline lens can modify the shape of the eye, changing the optical power of the eye as a whole. This forms the foundation of the accommodation process of the human sight, which enables the eye to concentrate on objects positioned at various distances. An elastic capsule covers the lens, which is joined to the ciliary body by zonules, a kind of ligament anatomical structure. The lens can change power by the contraction or the relaxation of the muscles in the ciliary body. Age-related decreases in close object focus are described

as presbyopia, at which point patients are unable to properly adjust the optical power of the lens in regard to the proximity of the object inside the field of view (LeGrand et al., 2013).

The clear vitreous humor-filled posterior chamber is the location where the light ends after being bent by the lens and before finally arriving to the retina. This is a thin layer of neural tissue that covers the back of the oculus and serves as a screen for the formation of pictures and the electrochemical transformation of the light signal. The fovea is the core region in the anatomy of the human retina where photoreceptors are located in a close formation to produce the highest possible resolution. In order to best focus the optical information into the fovea, the eyes move continually. Although the retina's periphery produces images with poorer quality, it can detect both an object and movement detection in the visual field. When compared to most artificial optical systems, the normal eye's field of view is relatively broad, measuring at least 160 degrees by 130 degrees (Smith et al., 2008).

The essential geometrical and optical details of the eye are shown schematically in Figure 1. These numbers must be interpreted as average values for the distances (in red), curvature radii (in black), and refractive indices (in blue).

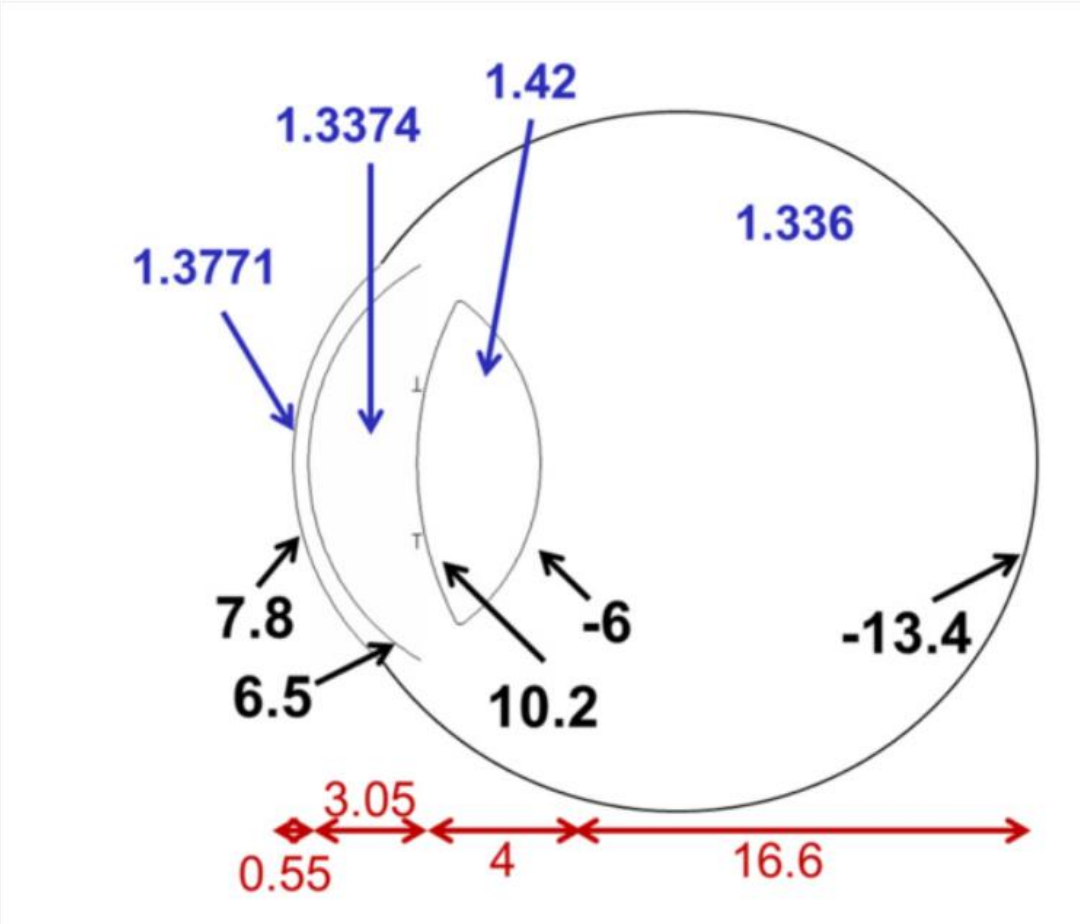

Figure 1. *The essential geometrical and optical details of the eye are shown schematically. Distances (red), curvature radii (black), and refractive indices (blue) in millimeters (Source: Artal et al., 2014).*

The cornea has a refractive index of 1.3771, an anterior radius of curvature of 7.8 mm, a posterior radius of curvature of 6.5 mm, and is roughly spherical in shape. This is responsible for the majority of the refractive power of the eye, approximately 70%, because the biggest variation in refractive index occurs from the air to the cornea (tear film). The anterior and posterior surfaces of the biconvex lens have radii of curvature of 10.2 and 6.0 mm, respectively. The layering of the lens's internal structure results in a non-homogeneous refractive index that has an equivalent value of 1.42 and is greater in the center in comparison to its periphery. Furthermore, the aqueous and vitreous humors have refractive indices of 1.3374 and 1.336, respectively (Tabernero et al., 2007).

An average eye will have an axial length of 24.2 mm and will be able to picture objects in distance exactly in focus onto the retina at these distances: 3.05, 4, and 16.6 mm for the anterior chamber, lens, and posterior chamber, respectively. Emmetropia is the term for this perfect circumstance where no pathologies or defects are present. However, the majority of eyes suffer from optical refractive defects and lack the necessary optical characteristics and proportions to attain perfect focus. The pictures created in the retina in these circumstances are hazy, often enforcing a lower threshold for visual perception. Myopia, which occurs when pictures of distant things are concentrated in front of the retina, and hypermetropia, which occurs when images of distant objects are focused behind the retina, are two types of refractive errors (Tabernero et al., 2007).

The common problem of astigmatism, which results in the retinal picture of a point source consisting of two perpendicular lines at various focus distances, is a frequent expression of these facts. The eyes do not create flawless pictures even in the event of no refractive defects, defocuses, or astigmatism. The main reason is the fact that in high-order optical aberrations, the retinal picture of a point source would not be another point but rather a broad distribution of light.

Since the ocular surfaces are not spherical in form and are not precisely aligned, the eye is not considered a centered optical system, unlike most artificial systems. The lens can also be tilted

and/or decentered with regard to the cornea, and the fovea. The region of the retina with the best image resolution, is decentered temporally (on average approximately 5 deg) (Figure 2).

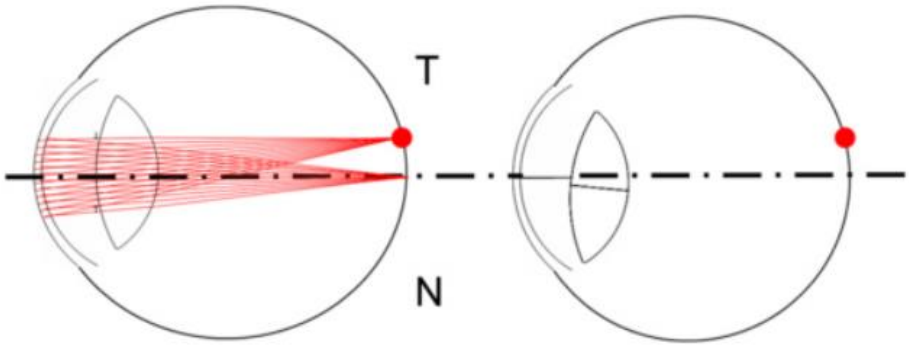

Figure 2. *Examples of the fovea (shown by the red circle) being beyond the optical axis and the crystalline lens possibly being decentered or tilted (in the right figure) (Source: Artal et al., 2014).*

3. Angle and axis in the eye

The definitions of the axes and angles involved in the eye need have been depicted in the preview paragraph in Figure 2. There are several definitions found in literature regarding taxis and angles in the human eye. One of the most commonly used is the Le Grand and El Hage's definition (Figure 3).

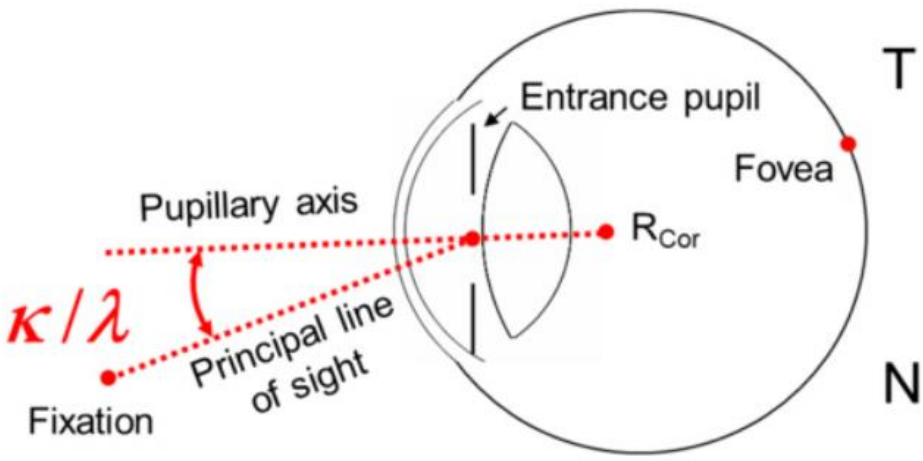

Figure 3. *The primary axes and angles that are frequently used in literature to characterize the eye depicted schematically (Source; Artal et al., 2014).*

Since the eye lacks an optical axis, two axes are established, that are connected to certain physiological characteristics. The imaginary line that crosses the entrance pupil's center perpendicular to the cornea is known as the pupillary axis. The line of sight runs from the center of the entry pupil to the fixation point in object space (and the center of the exit pupil with the fovea). These axes (line of sight and pupillary axis, respectively) can be thought of as approximate representations of the optical axis and the visual axis of the eye. Furthermore, it should be noted that the visual axis connects the fixation point to the fovea via the nodal points (Smith et al., 2008).

The angle kappa (κ) is the angle (in object space) between the pupillary axis and the line of sight. It should be noted that this is also frequently referred to as angle lambda (λ) in the literature. The fact that the same angle is referred to in the literature under the terms kappa and lambda is often confusing.

Additionally, the incident rays can be regarded as paraxial, which means that they have very tiny angles of incidence and are perpendicular to the optical axis (Fig. 4). A group of paraxial rays come together to form one point of focus. The incidence angles of the marginal rays increase as the diameter of the bundle of rays increases, rendering them nonparaxial. Figure 4 shows how spherical aberration causes these rays to cross the axis at various positions, obscuring the image. The eye's maximal pupil diameter of 2 mm is consistent with mathematical paraxial hypotheses (Smith et al., 2008).

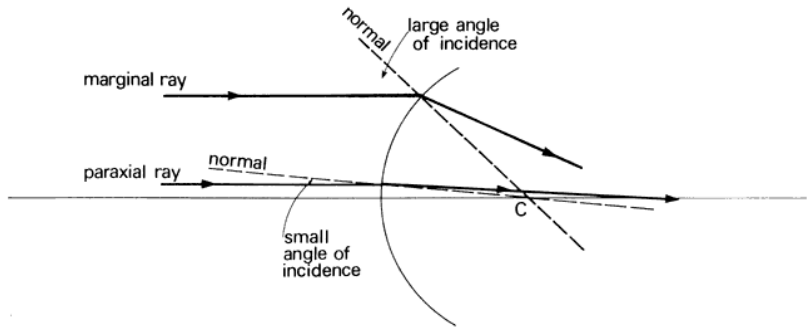

Figure 4. *Schematic representation of rays hitting a spherical surface at higher and higher altitudes above the optical axis have a rising angle of incidence.*

4. Historical perspective

Since the time of the ancient Greeks, the nature of the ocular picture has been a research objective. Galen, postulated that a psychological spirit entered the anterior chamber of the eye by a hollow optic nerve, traveled to the retina, and then exited as rays that illuminated things in space. The primary receptor that generated the visual perception and sent it back to the brain via the optic nerve as a visual spirit was the crystalline lens. Up until the Renaissance, Galen's beliefs were adopted by the scientific world across Europe. Optics research saw a lot of activity throughout the Renaissance. The use of spectacles to correct eyesight, the invention of the telescope and microscope, and the gradual growth of the idea that the eye functions like a pinhole camera all contributed to research conducted in this historical time. The biggest challenge, though, was trying to explain how the inversion aspect of the image perception (Pedrotti et al., 2017).

Huygens, struggled to create an optical model of the eye because to the scarcity of good data, even as late as the 17th century. Listing (1808–1882) created a schematic of an eye in 1851, but Helmholtz, who also developed the ophthalmometer and the ophthalmoscope (both were individually developed by Babbage as well), made significant strides in measuring the dioptrics of the eye. The primary challenges Helmholtz faced included getting precise information regarding the crystalline lens. Tscherning's invention, the ophthalmophacometer, allowed for the formation and alignment of distinct Purkinje pictures of all refracting surfaces at various obliquity angles (Pedrotti et al., 2017).

The Helmholtz schematic eye was improved by Gullstrand. More specifically, Gullstrand created the photokeratoscope, which he utilized to capture a target made up of concentric circles as it was reflected off the cornea. Circle spacing measurements in the picture could be used to determine if the cornea is spherical, aspheric, or astigmatic. Also, the cornea is astigmatic, or toroidal, if the images are elliptic. Additionally, the cornea's periphery could be examined, and its complete contour could be traced. The slit light, created by Gullstrand, made it easier to estimate depth or thickness. Gullstrand created an accurate optical model of the eye using these technological advancements, consisting of six spherical refracting surfaces: two for the cornea and four for the crystalline lens (Parker et al., 2011).

New methods for in vivo ocular measurements have been developed throughout the 20th century. A thin sheet of x-rays was directed in a coronal portion perpendicular to the visual axis of the dark-adapted eye by Rushton using a roentgenologic approach. Because the x-ray

beam is "slicing" across the eye, the phosphene, or sense of light, that is produced seems round. The section diameter shrinks as the beam moves near the eye's posterior pole, and the individual experiences a constricted, circular phosphene. The phosphene disappears when one reaches the posterior pole. Rushton was able to gauge the eye's axial length in this manner. The depth of the ocular components can also be measured using echography or ultrasonography. High-frequency sound waves are also used to quantify the amount of time it takes for them to pass through and reflect off the cornea, lens, and fundus's numerous surfaces. Distance is calculated using the formula distance = velocity x time. Measurements on cadavers are used to estimate media velocity.

Before using the roentgenologic approach, there was no means to measure the axial length of living eyeballs. Bu utilizing, this technique, Stenstrom conducted a statistical analysis of the eye's length and its relationship to other optical components. Despite the fact that hundreds of thousands of optical constant measurements have been performed, researchers only focused on a few numbers of factors in populations of various sizes and kinds. When all of these components are researched in the same participants, Stenstrom stressed the significance of discovering connections between all of the different dioptric parts of the eye (Stenstrom et al., 1948).

The two most crucial factors in defining the refractive state are the corneal refracting power and the length of the live eyeball. Stenstrom was interested in the determination of the axial length and its variation in different refractive states. His research showed that while the axial length greatly varied from a normal distribution, the lens refracting power, total refracting power, and corneal radius may be regarded normal distributions for individual optical elements. Additionally, Stenstrom discovered a tiny connection between the optical components, which reduced the dispersion of the overall refractive power compared to what would happen if the optical components fluctuated independently of one another. Also, the refractive error is unrelated to the depth of the anterior chamber, the radius of the cornea, the refracting power of the lens, and the overall refracting power of the eye. However, the axial length of the eye had a strong link with refractive error, which was later interpreted as evidence that the axial length is the most crucial factor affecting refractive error (Dariggol et al., 2012).

5. Basic optics geometry

5.1 Focal points and focal lengths

The collimated paraxial rays will converge to F', the second focal point, when light from an indefinitely distant source is discovered to the left of an optical element. For positive components, this will serve as a real image point, while for negative elements, it will serve as a virtual image point (Figures 5,6). The second focal length is the separation F'A. The optical component will collimate light coming from the initial focal point F, creating an image at infinity. The initial focal length is FA. The concept of vergence is derived from the concept of refractive power, which is taken from focal length (Tasman et al., 2005).

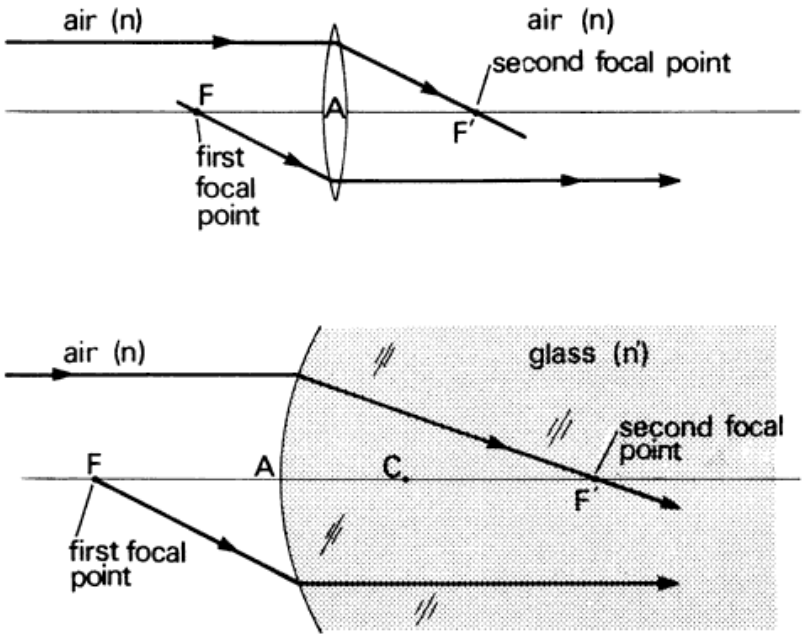

Figure 5. *Positions of the first and second focus points created by a positive single refracting surface and a positive thin air lens. For the narrow lens, the distance from F to A equals the distance from A to F'. For a single reflecting surface, the distance from C (the center of curvature) to F' is equal to the distance from F to A (Source: Tasman et al., 2005).*

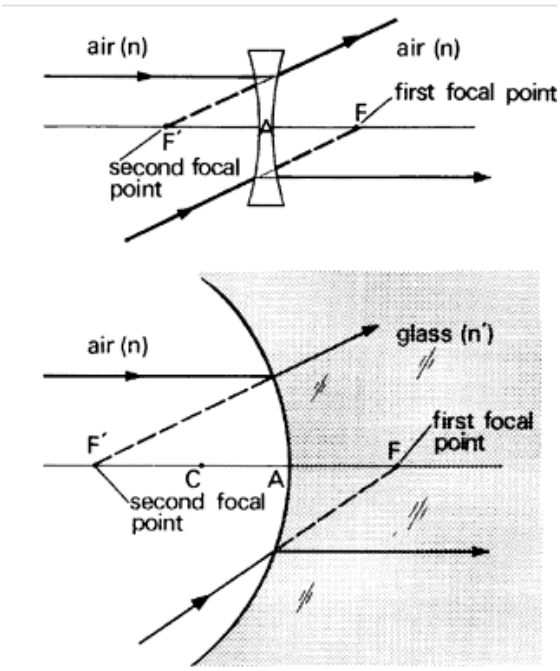

Figure 6. *A negative thin lens in the air and a negative single refracting surface together produce the first and second focal points in their respective positions (Source: Tasman et al., 2005).*

5.2 Vergence

As shown in Figure 7, the light that is diverging from an object point exhibits negative vergence. The spherical wavefronts enlarge respectively with increasing radial separation from the source. Since curvature is equal to the reciprocal of curvature's radius, the wavefront's curvature will be decreased, the further it is from an object (Perdoti et al., 2008).

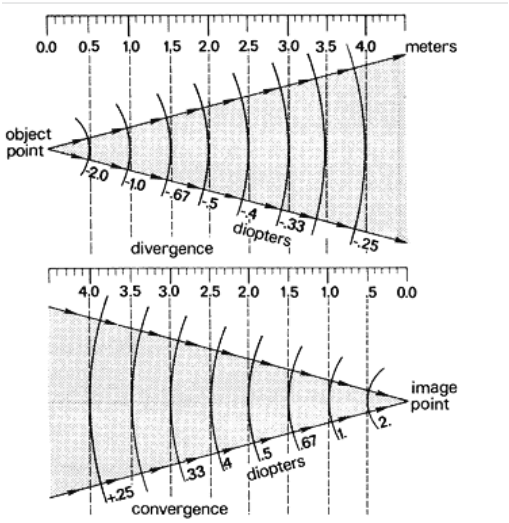

Figure 7. *Vergence measured in diopters and shown in proportion to a meter scale. Light departs from the object point and converges on the image point. The further the wavefronts are from any of these object points, their curvatures and the dioptric values of their vergences are shallower and weaker respectively (Source: Davidson et al., 2005).*

The reciprocal of the radial distance in meters is wavefront vergence in diopters:

Vergence = 1/Distance in meters

Positive vergence describes light that is approaching a picture and converges. As the wavefronts get closer to the picture point, they start to curve more and more, and the vergence rises along with it. For instance, the vergence is 14 = + 0.25 D at a distance of 4 meters and 12 = + 0.5 D at a distance of 2 meters.

Distances between objects and pictures in medium with any refractive index are shortened. The decreased distance for objects is l/n, while the reduced image distance is l'/n'. Similar to the first focal length, the second focal length is also lowered, becoming f'/n'. Decreased vergence is equivalent to reduced distance in the same way that vergence is the reciprocal of distance. The object's reduced vergence is L = n/l, while the image's reduced vergence is L' = n'/l'.

Incident light can be made to have a vergence using optical components. The reciprocal of the shortened focal length, or F = n/f = n'/f', is the refractive power F (not to be confused with the initial focal point, F). A relatively straightforward equation links the lowered vergence of the object and image to the refracting power: L' + L+F (Pedroti et al., 2008).

5.3 Nodal Points

Axial points are very useful in the calculation of the picture size. An incident ray would seem to emanate from the second nodal point with the same direction as it was before. Thus, the nodal points are referred to as points of unit angular magnification as a result. The first and second nodal points coincide with the first and second main points when the object and image are both in a medium with the same index of refraction (Figure 8a), a lens system surrounded by air. The main and nodal points all coincide at the lens's vertex if it's a straightforward thin lens in a homogeneous medium (Figure 8a). However, the nodal points do not correspond with the primary points if the image is not in the same medium as the object, as in the case of

the single refracting surface in Figure 8b. The two primary points and the two nodal points are located at the surface's vertex and the curve's center, respectively. In each of these instances, the ray's slope that is directed toward the first nodal point and the ray's slope that seems to emanate from the second nodal point are the same (Linden et al., 2012).

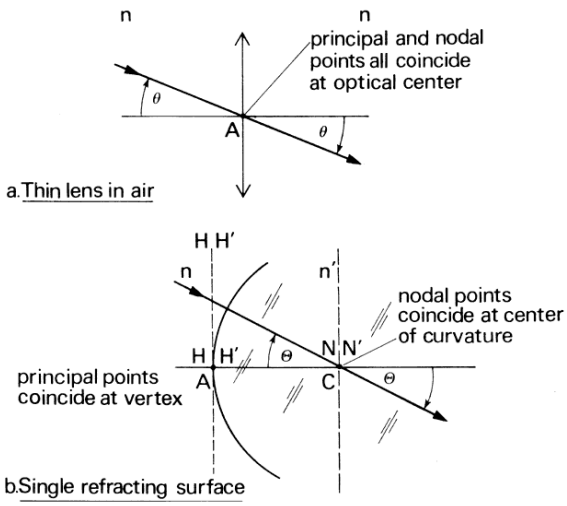

Figure 8. *The connection between the primary and nodal sites. a. Thin lens: At the optical center, H, H', N, and N' coincide. b. A single reflecting surface with the properties that H and H' coincide at the vertices and N and N' coincide at the curvature's center (Source: Davidson et al., 2008).*

6. Refracting Eye Models

To comprehend how the numerous refracting surfaces of the eye function, the optical models that have been developed are useful tools. These models are utilized in a variety of ophthalmic procedures, including as laser-assisted in situ keratomileusis, photorefractive keratectomy, optometry, and intraocular lens implantation. Schematic eyeballs help educators recognize, classify, and diagnose tendencies relating to age, gender, ethnicity, and accommodations in addition to offering insight into the optical properties of the eye. Model eyes can also be useful for comprehending how anatomical changes impact the development of some illnesses, such as myopia (Artal et al., 2014).

Over the past 150 years, several studies have focused on the behavior of the human eye, an anatomical structure that is described as an interesting optical instrument. The cornea, pupil,

lens, and retina construct the multiple-element refractive imaging system that is the human eye. The distinctive characteristics of the eye frequently behave as a virtually aplanatic system, where the lens's shape and gradient refractive index distribution may aid to lessen spherical and coma aberrations that originate in the cornea. Analogs to complicated wide-field imaging lenses may be drawn thanks to their optical properties (Jaeken et al., 2012). However, it is also crucial to model the many nuances of the human eye's optical characteristics in order to comprehend how they affect visual perception (La Rocca et al., 2013).

Thus, as expected, no optically precise wide-field schematic eye has been developed to assist in the design of contemporary imaging systems. High-resolution imaging modalities, such as optical coherence tomography, scanning laser ophthalmoscopy, and fluorescence imaging, may be able to extend their field of view to the peripheral retina if there is a robust model eye that can be used to potentially preemptively correct the aberrations inherent to the peripheral optics during a system's design. Numerous ocular disorders affect the peripheral retina, including Coats' disease, familial exudative vitreoretinopathy, retinal vein occlusions, choroidal dystrophies, vasculitis, uveitis, retinal tears and detachments, and incontinentia pigmenti (Williams et al., 1996, Atchison et al., 2002).

Early eye models were created by Moser (1844) and Listing (1851) utilizing schematic eyeballs with spherical surfaces for the cornea and lens. Helmholtz and Tscherning's work helped to further develop these models before the widely used Gullstrand model was presented in 1909. The Gullstrand model used a shell structure as the crystalline lens and was physically similar to actual eyes. However, because it was challenging to trace refracted light via a shell structure, Le Grand and Emsley eventually simplified the initial model. With the development more sophisticated techniques used to test the optical quality of the eye, modern eye modeling started to take shape in the late 20th century.

More specifically, in 1971, Lotmar enhanced the eye models by incorporating aspheric surfaces, while Kooijman and Pomerantzeff looked into the implications of a curved retina. In 1980, Blaker adopted an adaptable model of the human eye, and in 1991, he continued his research with a model that takes into account accommodation and aging. Axial chromatic aberrations and on-axis spherical aberrations were modeled by Thibos et al (Artal et al., 2010). Next, Liou and Brennan introduced a finite eye with a GRIN (Gradiate Refractive Index) lens that was inspired by anatomical structures. Escudero-Sanz and Navarro created a wide-field schematic eye by combining an accommodation-dependent mode with a curved imaging surface. Finally, using a decentered and slanted lens and retina, Atchison made a contribution,

but he also noted that the asymmetric model had trouble simulating the peripheral refraction of the eye. Soon after, customized eyes made for certain groups started to appear, with models developed by Navarro et al., Tabernero et al., and Rosales and Marcos. Later, Goncharov and Dainty added a GRIN lens to their initial schematic eyes that had a wide field, resulting in three different age-specific models (Polans et al., 2015).

6.1 Reduced eye – Single Refracting Surface

Calculations are made easier by considering the Gullstrand and contemporary schematic eyes as a black box and utilizing the cardinal points to establish object-image correlations due to the fact that both of these more recent models have six refracting surfaces. Listing calculated the decreased eye, a simplified eye model that is widely accepted. The eye model was simplified to a single refracting surface, the nodal point of which is located at the center of curvature and whose vertex coincides with the primary plane (Figure 9). This idea is supported by the fact that the two main locations in the anterior chamber that are in the middle of this structure, are barely separated by a millimeter and barely move at all during accommodation. Similarly, the two nodal points are positioned towards the posterior surface of the lens and have equal proximity as well (Atchison et al., 2016, Doshi et al., 2001).

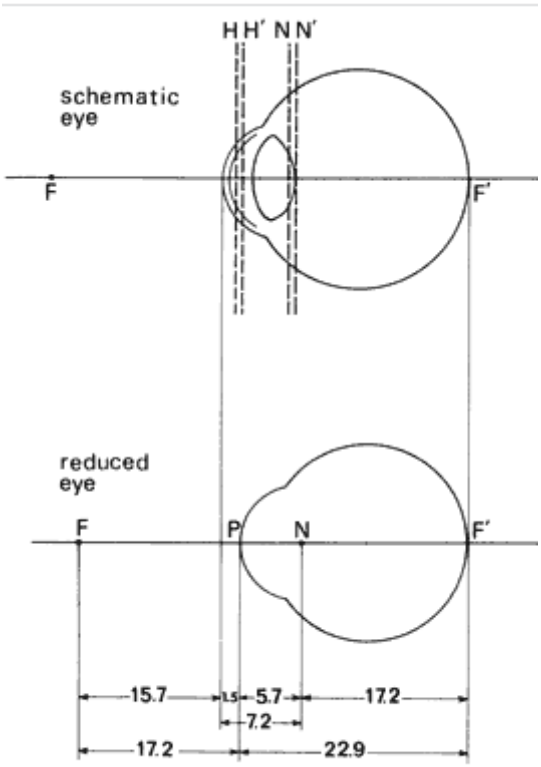

Figure 9. *Comparison between the schematic and the reduced eye models. In the latter model, the hypothetical surface that sits in the middle of the major points of the schematic eye is the refracting surface of the reduced eye (Source: Davidson et al., 2008).*

The main idea of the model is supported by the fact that the two main locations in the anterior chamber that are in the middle are barely separated by a millimeter and barely move at all during accommodation. The two nodal points also remain fixed close to the lens's posterior surface and are equally close together. The two principle points and the two nodal points were unified into one principal and nodal point in Listing's model. The main principal point is located 1.5 mm behind the cornea, and it depicts the center of a single, 5.7 mm-radius-curved refracting surface. The nodal point is 1.5 + 5.7 = 7.2 mm behind Gullstrand's calculations, because the nodal point of a single refracting surface is in the center of its curvature. The imaginary refracting surface of the reduced eye is 1.5 mm behind the cornea; hence Listing's reduced eye is 24.4 - 1.5 = 22.9 mm long. The emmetropic schematic eye measures 24.4 mm from the cornea to the fovea and has a homogeneous refractive index of 1.336 (Atchison et al., 2016, Doshi et al., 2001).

The nodal point remains in the center of curvature of this single refracting surface, making it relatively simple to estimate the sizes of retinal images. Object and image share the same angle because a beam from the tip of an object pointed at the nodal point would go straight to the retina without any deviation. The retinal picture size is calculated by multiplying the angle the object subtends in radians by the distance from the nodal point to the retina (17.2 mm).

The most famous example of this model is Emsley's reduced eye, which has a power of 60 D and a refractive index of 4/3 (or 1.33•), created by a corneal radius of curvature of 50/9 mm (or 5.55• mm). Although it has an inherent aperture stop, this may be positioned at the cornea or just within the eye. The decreased eye serves as an effective introduction to ocular chromatic aberrations and their consequences on vision by allowing the model's refractive index to change with wavelength.

$$M = \begin{pmatrix} 1 & D \\ 0 & 1 \end{pmatrix} \cdot \begin{pmatrix} 1 & 0 \\ -P & 1 \end{pmatrix} =$$

Where **P**=$\frac{n_{aqueous\ humor} - n_{air}}{R}$ = $\frac{1{,}33-1}{50/9} = 0{,}06mm$, ***Focal depth***: $\boldsymbol{d} = \frac{n}{P} = \frac{1{,}33}{0{,}06} = 22mm$ *and* $\boldsymbol{D} = \frac{d}{n_{aqueous\ humor}} = \frac{22}{1{,}33} = 16{,}5mm$

6.2 Simplified Eyes – Three refracting surfaces

Gullstrand's number 2 eye was altered by Emsley (1952) to make calculations easier (Figure 16.5 and Tables 16.7 and 16.8). The lens refractive index changed to 1.416, the lens was thicker, and the accommodated version had lens surface radii of curvature of 5.00 mm. The aqueous and vitreous refractive indices also changed to 4/3. For estimates of refractive error and accommodation, this model is used since more sophisticated models frequently don't offer much in the way of further benefits (Figure 10) (Atchison et al., 2016, Artal et al., 2017).

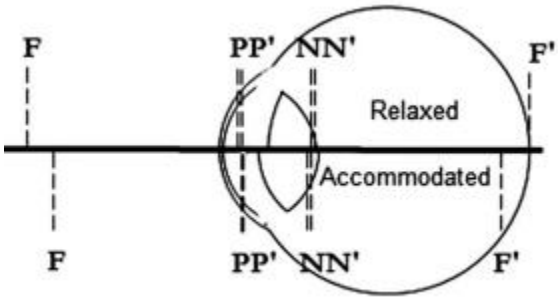

Figure 10. *Gullstrand–Emsley simplified eye model*

The equations for the Gullstrand–Emsley simplified eye model are:

$\frac{L}{n}$, $P_2=\frac{n_{air}-n}{-R}$, $P_1=\frac{n-n_{air}}{R}$

The matrix of the following optical system is the same as the thin lens so:

$$M=\begin{pmatrix}1 & 0\\ -P_2 & 1\end{pmatrix}\cdot\begin{pmatrix}1 & D\\ 0 & 1\end{pmatrix}\cdot\begin{pmatrix}1 & 0\\ -P_1 & 1\end{pmatrix}=\begin{pmatrix}1 & 0\\ -P_2 & 1\end{pmatrix}\cdot\begin{pmatrix}1-DP_1 & D\\ -P_1 & 1\end{pmatrix}$$
$$=\begin{pmatrix}1-DP_1 & D\\ -P_2+DP_1P_2-P_1 & -DP_2+1\end{pmatrix}$$

$\boldsymbol{M_{11}}=1-DP_1$, $\boldsymbol{M_{12}}=D$, $\boldsymbol{M_{21}}=-P_2+DP_1P_2-P_1$, $\boldsymbol{M_{22}}=-DP_2+1$

The **total optical power** of the optical system:

$$\boldsymbol{P_{tot}}=-M_{21}=-(-P_2+DP_1P_2-P_1)=\frac{n_{air}-n}{-R}-\frac{L}{n}\cdot\frac{n_{air}-n}{R}\cdot\frac{n-n_{air}}{R}+\frac{n-n_{air}}{R}=\frac{1-n}{-R}-\frac{L}{n}\frac{(1-n)(n-1)}{R^2}+\frac{n-1}{R}=\frac{2(n-1)}{R}-\frac{L}{n}\frac{(1-n)(n-1)}{R^2}=\frac{(\boldsymbol{n-1})}{\boldsymbol{R}}\left[\boldsymbol{2}-\frac{\boldsymbol{L}}{\boldsymbol{nR}}(\boldsymbol{1}-\boldsymbol{n})\right]$$

The position of the **principal planes**:

$$\boldsymbol{Z_H} = \frac{1-M_{22}}{M_{21}} = \frac{1+DP_2-1}{M_{21}} = \frac{-\frac{L}{n}\cdot\frac{(1-n)}{R}}{\frac{(-n+1)}{R}\left[2-\frac{L}{nR}(1-n)\right]} = \frac{-\frac{\boldsymbol{L}}{\boldsymbol{n}}}{\left[\boldsymbol{2}-\frac{\boldsymbol{L}}{\boldsymbol{nR}}(\boldsymbol{1}-\boldsymbol{n})\right]}$$

$$\Rightarrow \boldsymbol{Z_H} = \frac{z_H}{n} \Rightarrow \boldsymbol{z_H} = \frac{-\frac{\boldsymbol{L}}{\boldsymbol{n}}}{\left[\boldsymbol{2}-\frac{\boldsymbol{L}}{\boldsymbol{nR}}(\boldsymbol{1}-\boldsymbol{n})\right]}\cdot\boldsymbol{n}$$

$$\boldsymbol{Z'_H} = \frac{1-M_{11}}{M_{21}} = \frac{1-1+DP_1}{M_{21}} = \frac{\frac{L}{n}\cdot\frac{n-1}{R}}{-\frac{(n-1)}{R}\left[2-\frac{L}{nR}(1-n)\right]} = \frac{\frac{L}{n}}{-\left[2-\frac{L}{nR}(1-n)\right]}$$

$$\Rightarrow \boldsymbol{Z'_H} = \frac{z_H{}'}{n} \Rightarrow \boldsymbol{z'_H} = \frac{\frac{\boldsymbol{L}}{\boldsymbol{n}}}{-\left[\boldsymbol{2}-\frac{\boldsymbol{L}}{\boldsymbol{nR}}(\boldsymbol{1}-\boldsymbol{n})\right]}\cdot\boldsymbol{n}$$

$\boldsymbol{z_H}, \boldsymbol{z_H}'$ →**actual value** (actual distance) , $\boldsymbol{Z_H}, \boldsymbol{Z_H}'$ →**reduced distance**

The position of the **foci**:

$$\boldsymbol{f} = \frac{n_s}{P_{tot}} = \frac{\boldsymbol{1}}{\frac{(\boldsymbol{n}-\boldsymbol{1})}{\boldsymbol{R}}\left[\boldsymbol{2}-\frac{\boldsymbol{L}}{\boldsymbol{nR}}(\boldsymbol{1}-\boldsymbol{n})\right]}$$

$$\boldsymbol{f'} = \frac{n_s{}'}{P_{tot}} = \frac{\boldsymbol{1}}{\frac{(\boldsymbol{n}-\boldsymbol{1})}{\boldsymbol{R}}\left[\boldsymbol{2}-\frac{\boldsymbol{L}}{\boldsymbol{nR}}(\boldsymbol{1}-\boldsymbol{n})\right]}$$

So, the **effective focal length** (**EFL**):

$$(\boldsymbol{EFL}) = f + z_H = \frac{\boldsymbol{1}}{\frac{(\boldsymbol{n}-\boldsymbol{1})}{\boldsymbol{R}}\left[\boldsymbol{2}-\frac{\boldsymbol{L}}{\boldsymbol{nR}}(\boldsymbol{1}-\boldsymbol{n})\right]} - \left(\frac{\frac{\boldsymbol{L}}{\boldsymbol{n}}}{\left[\boldsymbol{2}-\frac{\boldsymbol{L}}{\boldsymbol{nR}}(\boldsymbol{1}-\boldsymbol{n})\right]}\cdot\boldsymbol{n}\right)$$

Back focal length (**BFL**):

$$(\boldsymbol{BFL}) = f' + z'_H = \frac{\boldsymbol{1}}{\frac{(\boldsymbol{n}-\boldsymbol{1})}{\boldsymbol{R}}\left[\boldsymbol{2}-\frac{\boldsymbol{L}}{\boldsymbol{nR}}(\boldsymbol{1}-\boldsymbol{n})\right]} - \left(\frac{\frac{\boldsymbol{L}}{\boldsymbol{n}}}{\left[\boldsymbol{2}-\frac{\boldsymbol{L}}{\boldsymbol{nR}}(\boldsymbol{1}-\boldsymbol{n})\right]}\cdot\boldsymbol{n}\right)$$

6.3 Model with four refracting surfaces

These models have two refracting surfaces for the lens and the cornea. Le Grand's entire theoretical eye, which is available in relaxed and 7.1 D accommodated variants, is a nice

illustration (Figure 11). The lens becomes more curved, the front surface advances by 0.4 mm, and the posterior surface recedes by 0.1 mm to transition from the relaxed to the accommodated form. These models have led to the development of "adaptive" optical model eyes, with equations illustrating how parameters change with age and accommodation (Artal et al., 2017).

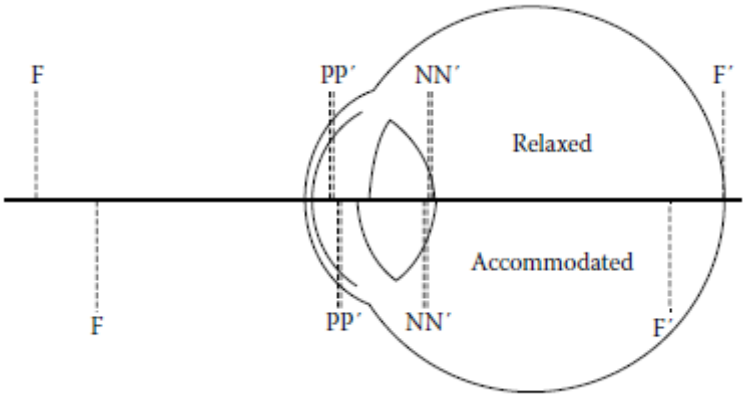

Figure 11. *Schematic representation of Le Grand's theoretical eye (Source et al., 2017).*

The equations in which the calculations for this model are based are:

$D = \frac{d}{n_{glass}} = \frac{2R}{n_{glass}}$, $P_1 = \frac{n_{glass} - n_{air}}{R}$, $P_2 = \frac{n_{water} - n_{glass}}{-R}$

The matrix of the following optical system is the same as the thin lens so:

$$M = \begin{pmatrix} 1 & 0 \\ -P_2 & 1 \end{pmatrix} \cdot \begin{pmatrix} 1 & D \\ 0 & 1 \end{pmatrix} \cdot \begin{pmatrix} 1 & 0 \\ -P_1 & 1 \end{pmatrix} = \begin{pmatrix} 1 & 0 \\ -P_2 & 1 \end{pmatrix} \cdot \begin{pmatrix} 1 - DP_1 & D \\ -P_1 & 1 \end{pmatrix}$$
$$= \begin{pmatrix} 1 - DP_1 & D \\ -P_2 + DP_1P_2 - P_1 & -DP_2 + 1 \end{pmatrix}$$

$\boldsymbol{M_{11}} = 1 - DP_1$, $\boldsymbol{M_{12}} = D$, $\boldsymbol{M_{21}} = -P_2 + DP_1P_2 - P_1$, $\boldsymbol{M_{22}} = -DP_2 + 1$

The **total optical power** of the optical system:

$$\boldsymbol{P_{tot}} = -M_{21} = -(-P_2 + DP_1P_2 - P_1) = -\frac{n_{water} - n_{glass}}{R} - \frac{2R}{n_{glass}} \cdot \frac{n_{glass} - n_{air}}{R} \cdot$$
$$\frac{n_{water} - n_{glass}}{R} + \frac{n_{glass} - n_{air}}{R} = -\frac{\frac{4}{3} - \frac{3}{2}}{R} + \frac{2R}{\frac{3}{2}} \cdot \frac{\frac{3}{2} - 1}{R} \cdot \frac{\frac{4}{3} - \frac{3}{2}}{R} + \frac{\frac{3}{2} - 1}{R} = +\frac{3}{18R} - \frac{2}{18R} + \frac{9}{18R} = \frac{10}{18R} = \boldsymbol{\frac{5}{9R}}$$

The position of the **principal planes**:

$$\boldsymbol{Z_H} = \frac{1-M_{22}}{M_{21}} = \frac{1+DP_2-1}{M_{21}} = \frac{\frac{2R}{n_{glass}} \cdot \frac{n_{water}-n_{glass}}{R}}{-\frac{5}{9R}} = \frac{-\frac{2R}{\frac{3}{2}} \cdot \frac{\frac{4}{3}-\frac{3}{2}}{R}}{-\frac{5}{9R}} = \frac{\frac{4}{18}}{-\frac{5}{9R}} = -\frac{36R}{90} = -\boldsymbol{\frac{6R}{15}}$$

$$\Rightarrow \boldsymbol{Z_H} = \frac{z_H}{n_{glass}} \Rightarrow \boldsymbol{z_H} = \frac{3}{2} \cdot \frac{6R}{15} = -\boldsymbol{\frac{18R}{30}}$$

$$\boldsymbol{Z'_H} = \frac{1-M_{11}}{M_{21}} = \frac{1-1+DP_1}{M_{21}} = \frac{\frac{2R}{n_{glass}} \cdot \frac{n_{glass}-n_{air}}{R}}{-\frac{5}{9R}} = \frac{\frac{2R}{\frac{3}{2}} \cdot \frac{\frac{3}{2}-1}{R}}{-\frac{5}{9R}} = -\frac{\frac{4}{6}}{\frac{5}{9R}} = -\frac{36R}{30} = -\boldsymbol{\frac{6R}{5}}$$

$$\Rightarrow \boldsymbol{Z'_H} = \frac{z_{H'}}{n_{glass}} \Rightarrow \boldsymbol{z'_H} = \frac{3}{2} \cdot -\frac{6R}{5} = -\boldsymbol{\frac{18R}{10}}$$

$\boldsymbol{z_H}, \boldsymbol{z_H}'$ →**actual value** (actual distance) , $\boldsymbol{Z_H}, \boldsymbol{Z_H}'$ →**reduced distance**

The position of the **foci**:

$$\boldsymbol{f} = \frac{n_s}{P_{tot}} = \frac{n_{air}}{P_{tot}} = \frac{1}{\frac{5}{9R}} = \boldsymbol{\frac{9R}{5}}$$

$$\boldsymbol{f'} = \frac{n_{s'}}{P_{tot}} = \frac{n_{water}}{P_{tot}} = \frac{\frac{4}{3}}{\frac{5}{9R}} = \boldsymbol{\frac{36R}{15}}$$

6.4 Models with lens structure

The crystalline lens's refractive index is not constant; rather, it is inhomogeneous, with a gradient index—an increase in refractive index—from the edge to the center. The overall refracting power of the lens is more than would be predicted from its surface powers because the gradient index has its own power apart from the surface powers. The lack of a gradient index has been made up for in the three and four refracting surface models, such the ones listed in the above paragraphs, by enhancing surface power by having a "equivalent" index. This index is significantly higher than the index that occurs in the real eye lens (Donggeul et al., 2017).

An early effort to model the gradient index of the eye was undertaken by the English scientist Thomas Young. Figure 12 depicts his refractive index function against optical axis location together with a parabolic curve more accurate and realistic.

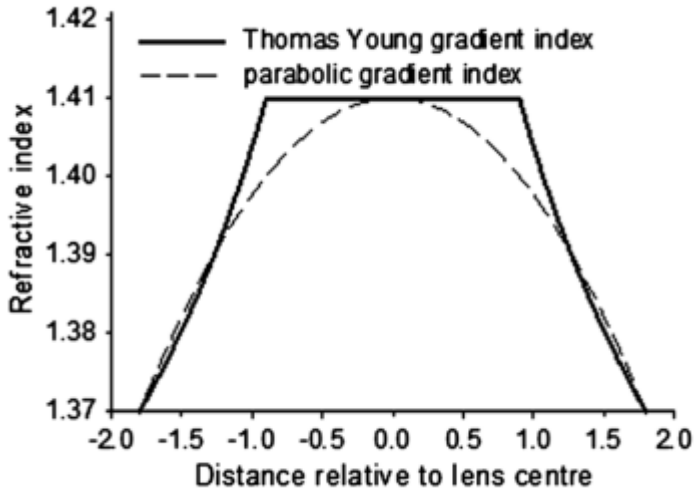

Figure 12. *Distribution of the refractive index based on Thomas Young's model. For comparison, a parabolic distribution is displayed (Source: Atchison et al., 2016).*

The lens models used in standard schematic eyes are the most prevalent. These eyes have lenses with spherical surfaces and a constant refractive index, apart from the Gullstrand number 1 eye. Even while these lenses reliably predict Gaussian characteristics like equivalent power, they predict less accurately the aberrations of the lens. There have been several attempts to create more realistic models The most prominent examples are the model proposed by Lotmar. Lotmar described a lens with a constant index and a back aspheric surface and found that this lens gave aberrations similar to those in real eyes. Later, Blaker described a spherically surfaced lens with a variable refractive index based on the Gullstrand lens while Kooijman presented a lens with a similar structural design; and many others (Katz et al., 2013).

Assuming rotational symmetry about the optical (Z) axis, the refractive index distribution N (Y, Z) in the YZ section may be represented in a generic manner as follows:

$$N(Y,Z) = N_0(Z) + N_1(Z)Y^2 + N_2(Z)Y^4 \ldots$$

with

$$N_0(Z) = N_{0,0} + N_{0,1}Z + N_{0,2}Z^2 + N_{0,3}Z^3 + N_{0,4}Z^4 \ldots$$

$$N_1(Z) = N_{1,0} + N_{1,1}Z + N_{1,2}Z^2 + N_{1,3}Z^3 + N_{2,4}Z^4 \ldots$$

$$N_2(Z) = N_{2,0} + N_{2,1}Z + N_{2,2}Z^2 + N_{2,3}Z^3 + N_{2,4}Z^4 \ldots$$

$$\ldots$$

These terms may be used to characterize the refractive index distributions that Gullstrand used to develop his number one eye relaxed and accommodated lenses in 1909, an eye model with four lens surfaces and two corneal surfaces (Katz et al., 2013). The iso-indical contours are also depicted in Figure 13.

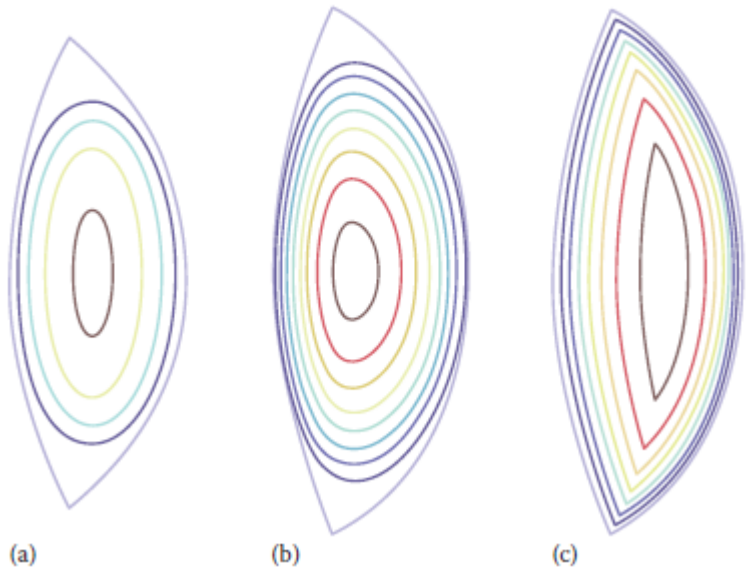

Figure 13. *Iso indical contours and lens shapes. (a) unaccommodated version of Gullstrand number 1 eye. Liou and Brennan eye. Navaro et al., eye (Source: Artal et al., 2017).*

Analyses are complicated by gradient index optics. In response, model eye creators in the 20th century used layered, homogeneous shells with various refractive indices to approximate the actual, gradient index nature of the lens. Gullstrand was the first scientist who created the

most reliable model of the eye. His approach was based on several previous studies as well as his own extremely innovative for this particular time period tests and instruments. The curvatures of the surfaces of the cornea and lens, their locations, and the indices of refraction of the ocular media were the crucial factors Gullstrand need to determine how light travels through the eye. The methods for making these findings, as described by Helmholtz and Gullstrand, involve extensive trigonometric computations and are experimentally challenging. The optical zone has physiologic astigmatism, which causes it to bend more sharply vertically than horizontally (Smith et al., 1991).

Although it seems to be spherical, the anterior surface of the cornea is in fact not this shape. On the contrary, the optical zone, which is 2 to 3 mm in diameter and centered on the vertex, is where the rays enter the eye. Furthermore, the optical zone has physiologic astigmatism, which causes it to bend more sharply vertically than horizontally. The anterior surface of the cornea asymmetrically flattens outward from this region. It could be asymmetric on the opposing sides of the vertex and less flat in some meridians (Smith et al., 1995).

Gullstrand's photokeratoscope, a tool that took pictures of the corneally reflected image of an illuminated pattern of circles, was used to identify these topographic characteristics of the anterior surface of the cornea. The corneal contour was determined using measurements taken from the images. This procedure also required the use of the ophthalmometer. Both techniques rely on reflections from the cornea's front surface. The first of the four Purkinje pictures is this reflection. Utilizing these techniques, it is possible to discern the reflex from the lens' anterior and posterior surfaces as well as a weak reflection from the cornea's posterior side. While the posterior lens surface is considered hollow and creates a true reflex picture of a faraway object, the anterior lens surface is convex and creates a virtual reflex image. These surfaces all function as straightforward spherical mirrors. Given that the optical properties of the optical components that precede each surface of interest are known, their radii can thus be computed with ease. Gullstrand had to take measurements of 14 ocular characteristics, including the indices of the media, the thicknesses of the components, and the curvatures of the surfaces. The optical constancies of Gullstrand’s number 1 eye are given in Figure 14 (Sen et al., 2021).

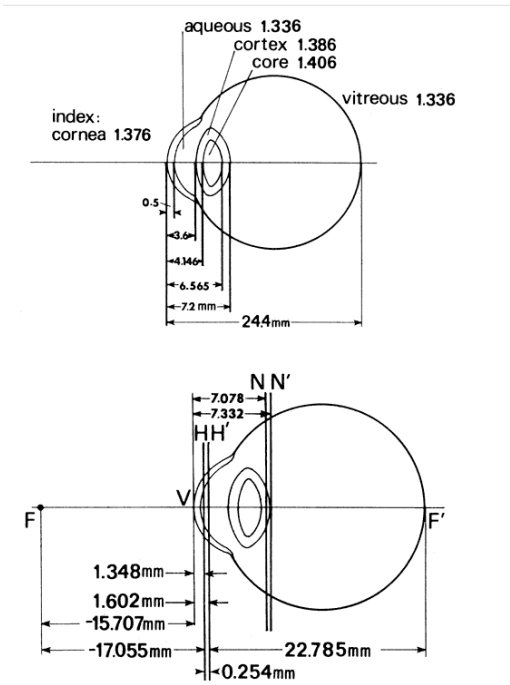

Figure 14. *Optical parameters of the model eye created by Gullstrand. Top: media indicators and the locations of the reflective surfaces. Bottom: the locations of the cardinal points, which act as the eye in optical computations (Source Sen et al., 2021).*

In the latest decades, substantial literature documenting the anatomy and optical characteristics of the human eye has been produced as a result of recent technical advancements in biometry. These include the lens' gradient index, the cornea's and the lens's aspheric surface curves, and the ocular media's dispersive properties. It is simple to assess the optical qualities, particularly the aberrations of model eyes having these attributes, helped by robust optical ray trace tools. Figure 15 depicts one such model that forecasts chromatic and spherical aberration and Table 1 lists the characteristics of its structural makeup (Liu et al., 1997).

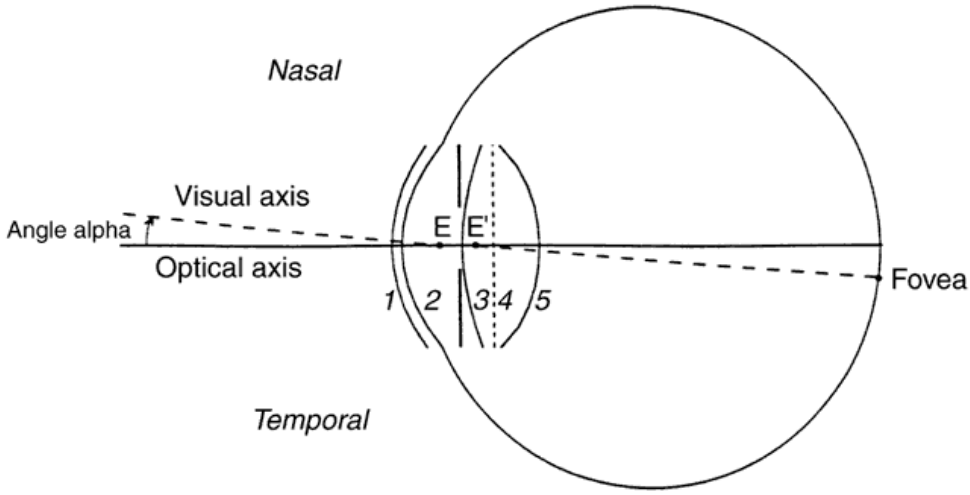

Figure 15. *Schematic representation of the modern eye model proposed by Liou and Brennan (Source: Liu et al., 1997)*

Table 1. Modern Schematic Eye

Surface	Radius (mm)	Asphericity Q	Thickness (mm)	Index at 555nm
Cornea 1	7,7	-0,18	0,50	1,367
Cornea 2	6,4	-0,60	3,16	1,336
Lens 1	12,4	-0,94	1,59	Grad A
Lens 2	Infinite	--	2,43	Grad B
Lens 3	-8,10	+0,96	16,27	1,336

The optical axis is the center of all surfaces. The aperture stop is 0.5 mm nasally decentered and corresponds with the front surface of the lens. An imaginary plane known as "lens surface 2" divides the lens into an anterior and posterior gradient index (Grads A and B). Defined between 0 and -1, asphericity Q values are ellipsoids about the main axis.

In the model proposed by Navaro, Gonzales and Palos, the point of interest (highest refractive index) was redeployed in toward the back of the lens. This approach has been proven experimentally, however, the shape of the lens is not anatomically accurate (Navaro et al., 2007). A similar model was also developed by Bahrami and Goncharov, who proposed a "geometric-invariant" refractive index structure, flattening the anterior and posterior surfaces and isoindical contours to meet seamlessly (Bahrami et al., 2012)

6.5 The development of finite optical models

Gullstrand's precise eye model as well as the later paraxial models had a two-shell structure to account for the variance in lenticular refractive index, but more subsequent efforts have been more complex. In order to simulate the gradient refractive index of the lens, Pomerantzeff et al. (1971) employed a series of shells. Al-Ahdali and El-Messiery (1995) used 300 of these shells, while later Liu et al. (2005), who used 602, have expanded on this strategy. From a mathematical perspective, Kasprzak (2000) suggested a novel approximation incorporating hyperbolic cosines for the whole profile of the human crystalline lens (Bakaraju et al., 2008).

Gradient refractive indices that are connected by two aspheric surfaces have superseded shell-structured lenses due to the development of ray tracing capabilities through gradient index media. It has been argued that a number of these finite, or wide angle, designs provide accurate predictions for both on- and off-axis aberrations. The most well-known instances under this heading are those of Escudero-Sanz and Navarro, 1999, Kooijman, 1983, Liou and Brennan, 1997, Lotmar, 1971, and Navarro et al., 1985, with a substantial number of being made for the specifications of the various surfaces. Escudero-Sanz and Navarro later conducted a thorough analysis of the off-axis aberrations of the unaccommodated variant of the Navarro, Santamaria, and Bescos (1985) model (1999) (Navaro et al., 1985, Escudero-Sanz et al., 1999).

The simpler, single reduced surface model proposed by Thibos and colleagues (Thibos, Ye, Zhang, & Bradley, 1992), and it was somewhat successful in that it successfully predicted spherical as well as chromatic aberrations of the eye. The problem still remains, however, that any reduced eye technique is constrained in terms of its capacity to accurately depict real-world vision since it is unable to take into account certain parameters such as the type of variation in refracting surfaces that happens naturally. In an effort to solve this issue, Siedlecki, Kasprzak, and Pierscionek (2004) combined a lens with aspheric surfaces and a more specific gradient index with the surface parameters developed previously by Kooijman (1983) (Thibos et al., 1982, Siedlecki et al., 2004, Koojiman et al., 1983).

Despite their claims of better picture quality and minimal spherical aberration for their wide-angle model, it appears that their work did not find widespread acceptance and is not one of the researchers that are frequently cited in the literature. Other models include accommodating changes for near (Goncharov and Dainty, 2007), lenticular refractive index modifications according to age (Goncharov and Dainty, 2007, Norrby, 2005), changing

refractive error using a more generic adult model (Popiolek-Masajada and Kasprzak, 2002), and models including accommodative changes for distant objects (Le Grand et al., 1980, Navarro et al., 1985).

Goncharov and Dainty (2007) further improved this by incorporating a mathematical model of a gradient-index (GRIN) lens and were able to replicate the characteristics of two previously proposed eye models: the Navarro's model for off-axis aberrations and the Thibos's chromatic on-axis model (Escudero-Sanz et al., 1999, Thibos et al., 1992). Even though, these numerous advancements have been impressive in helping the optic science to comprehend the optics of normal human eyes and to guide the design of visual optics, it is well acknowledged that their predictions for specific genuine eyes can be substantially inaccurate. Navarro et al. have recommended the creation of individualized eye models utilizing data specifically obtained for each individual to solve this issue (Navarro et al., 2006). Although the optimization technique they employed was effective and they managed to reliably replicate the total wavefront aberrations of the tested eyes, it had several limitations in terms of reproducing crystalline lens shape. Rosales et al., working with eyes that have intraocular lenses (IOLs), also used an individualized approach that had important consistency with in-vivo data. Their effort lends credence to the idea that the adoption of an improper lenticular gradient index profile limited Navarro et al previous attempt (Rosales et al., 2007).

A number of these novel finite model eyes are quite complex, encyclopedic in scope, and have gradient index distributions. Some scientific groups utilize "reverse engineering," in which other parameters are determined by using data from population measurements of on- and off-axis aberration and ocular biometry in combination with an optimization method in a specifically designed tool, usually a software tool. A finite model may be helpful for characterizing the functional capabilities of the eye even when the calculated parameters might not be physically precise. One of the most recently proposed models seems to be able to accurately approximate the mean aberration of the population that was used as a training set (Polans et al., 2015).

6.6 Refraction Eye models based on population

Most optical models have had generic eyes that represent averages in the population. Refractive error, gender, ethnicity, age and accommodation can be used to correct the model’s parameters for both clinically normal and pathological circumstances across the

corresponding populations. Table 2 summarizes a study on optical models for myopic and emmetropic eyes in a population of young adults and is an example of a population study. The models of this particular approach had a lens gradient index and four refracting surfaces. The table lists the models' parameters: asphericities, curvature radii, refractive indices, and internal distances. The depth of the vitreous chamber, the anterior radius of curvature of the cornea, and the asphericity and radius of curvature of the retina were all parameters that varied with refraction.

Table 2 Optical model ocular parameters as a function of dioptric refraction (SR) in spectacles. "r" is the distance, in either direction, between the lens's center and its edge (Source: Atchison et al., 2006)

Medium	**Refractive Index**	**Radius of Curvature**	**Asphericity**	**Distance to next surface (mm)**
Air	1,0	+7,77 + 0,022 SR		
Cornea	1, 376	+6,40		0,55
Aqueous	1,3374	+11,48		3,15
Anterior Lens	$1,71 + 0,037r^2$	Infinity		1,44
Posterior Lens	1,416 – 0,037r	-5,90		2,16
Vitreous	1,336	x: –12.91– 0.094 SR y: –12.72 + 0.004 SR	x: +0.27 + 0.026 SR y: +0.25 + 0.017 SR	
Retina	-	-	-	-

Thomas Young (1773–1829) was a pioneer in the study of the eye's accommodative system and one of the first scientists to propose a schematic eye for an individual. According to his model, the eye might theoretically alter its focus in several ways, including the alteration of its axial length could alter. In essence, this is the mechanics under which a camera focuses on close things. In extreme close-up photography, the lens is linked to a bellows that allows placing the lens within a much wider range. Alternatively, the lens is simply pushed farther from the film plane using a focusing ring integrated into the lens barrel. So, it only makes sense

to wonder if the eye lengthens to focus on close things. An item 10 cm away from the eye may be focused on with ease by a juvenile emmetrope. Young, after a number of difficult experiments on himself, he used a customized set of dividers with tiny rings at both points, to measure the length of his eyes. To the greatest extent feasible, Young reversed his eye, and the rings were positioned outside the macula and cornea. He also recorder the entoptic ring phosphene, which was created by the pressure at the back of the eye, in the center of his field of vision (Atchison et al., 2011).

To reach the final value of an internal axial length that equals 23.1 mm, he deducted 0.8 mm to account for the coats and thicknesses of the eyes. His eye is schematically depicted in Figure 16, together with the Gullstrand-Emsley model eye for comparison.

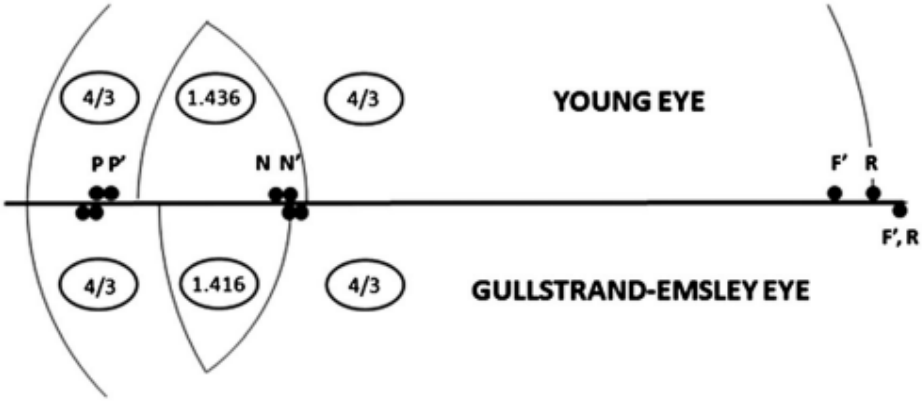

Figure 16. *Model based on the specifications of Thomas Young's left eye for comparison. The Gullstrand-Emsley eye is displayed on the latter section of the image for comparison. Media's refractive indices are shown as ellipses. The retina is indicated by R, and the cardinal points are P, P', F, F', N, and N' (Source: Atchison et al., 2010).*

7. Conclusions

Schematic eyeballs are representations of the human eye's optical-related biometry. These are often based on average population data that the authors have access to, which makes them prone to biases such refraction age, gender, range and race. Different levels of complexity may be achieved while developing schematic eyes. Calculations are made easier with the use of simple models, but these, simpler models can only approximate the optical capabilities of the human eye to a certain extent. On the other hand, complex models with several aspheric surfaces, refractive index gradients, surface tilts and misalignments, etc., may describe the eye's typical levels of aberration and off-axis optical performance considerably and more thoroughly but need far more complex computations to be performed.

The paraxial schematic eyes are one type of schematic eye, and they have spherical refractive surfaces that are centered on an optical axis. The media of these eyes often have uniform refractive indices; however, this is not always the case. Paraxial refers to the fact that these schematic eyes can only be taken into account for correctly representing the optics of actual eyes when rays are near to the optical axis and subtend minor angles to it. At big pupils or for angles more than a few degrees from the optical axis, they are unable to reliably forecast aberrations and the quality of the retinal picture.

The paraxial schematic eyes are one such type of schematic eye, and they have spherical refractive surfaces that are centered on an optical axis. In most of these models, the media of these eyes often have uniform refractive. Paraxial refers to the fact that these schematic eyes can perform accurate optic metrics for correctly representing the optics of actual eyes when rays are near to the optical axis and subtend minor angles to it. At big pupils or for angles that deviate more than a few degrees from the optical axis, they are unable to reliably model aberrations and the quality of the true retinal picture. The region that results in the least amount of inaccuracy when utilizing geometrical optics is defined in literature as the paraxial region. In clinical practice, this entails field angles of less than 2° and pupil diameters of less than 0.5 mm.

More realistic schematic eyes are necessary for anticipating aberrations or pathologies and the picture quality caused by such aberrations or pathologies. These models are defined as finite or wide-angle schematic eyes. One or more nonspherical refractive surfaces, a lack of surface alignment along a common axis, and media with wavelength-dependent refractive indices are a few examples of these models. Many of them are extensions of paraxial

schematic eyes and may be judged similarly to those by disregarding their embellishments. Although the majority of finite eyes are based on population averages, they may be modified to better characterize particular eyes.

The purpose of the current thesis was to summarize the most recent literature information, regarding the refractive eye models. More specifically, after providing some background information about the main reflection properties of the eye, and a brief historical overview, further elaboration is made regarding: the reduced eye model (single refractive surface), models with three and four refractive surfaces respectively, models that take into account the lens surface, finite optical models and refraction models that have adjusted parameters according to certain populations. Finally, some insight is provided regarding the selection of the most suitable model in clinical practice.

References

Artal, P., 2014. Optics of the eye and its impact in vision: a tutorial. *Advances in Optics and Photonics*, *6*(3), pp.340-367.

Atchison, D.A. and Thibos, L.N., 2016. Optical models of the human eye. *Clinical and Experimental Optometry*, *99*(2), pp.99-106.

Atchison, D.A. and Charman, W.N., 2010. Thomas Young's contribution to visual optics: The Bakerian lecture "On the mechanism of the eye". *Journal of vision*, *10*(12), pp.16-16.

Atchison, D.A. and Charman, W.N., 2011. Thomas Young's investigations in gradient-index optics. *Optometry and Vision Science*, *88*(5), pp.E580-E584.

Atchison, D.A., 2006. Optical models for human myopic eyes. *Vision research*, *46*(14), pp.2236-2250.

Atchison, D.A. and Scott, D.H., 2002. Monochromatic aberrations of human eyes in the horizontal visual field. *JOSA A*, *19*(11), pp.2180-2184.

Artal, P. and Tabernero, J., 2010. Optics of human eye: 400 years of exploration from Galileo's time. *Applied optics*, *49*(16), pp. D123-D130.

Artal, P., 2014. Optics of the eye and its impact in vision: a tutorial. *Advances in Optics and Photonics*, *6*(3), pp.340-367.

Artal, P., 2017. *Handbook of visual optics, two-volume set*. CRC Press.

Bakaraju, R.C., Ehrmann, K., Papas, E. and Ho, A., 2008. Finite schematic eye models and their accuracy to in-vivo data. *Vision research*, *48*(16), pp.1681-1694.

Bahrami, M. and Goncharov, A.V., 2012. Geometry-invariant gradient refractive index lens: analytical ray tracing. *Journal of Biomedical Optics*, *17*(5), p.055001.

Darrigol, O., 2012. *A history of optics from Greek antiquity to the nineteenth century*. OUP Oxford.

Davison, J.A., 2005. Chapter 11: Intraocular Lenses, Duane's Clinical Ophthalmology on CD-ROM.

Donggeul, H.Y.U.N. and Hunkoog, J.H.O., 2017. A Study on Modeling the Accommodation of the Human Eye for Science Education.

Doshi, J.B., Sarver, E.J. and Applegate, R.A., 2001. Schematic eye models for simulation of patient visual performance. *Journal of Refractive Surgery*, *17*(4), pp.414-419.

Escudero-Sanz, I. and Navarro, R., 1999. Off-axis aberrations of a wide-angle schematic eye model. *JOSA A*, *16*(8), pp.1881-1891.

Jaeken, B. and Artal, P., 2012. Optical quality of emmetropic and myopic eyes in the periphery measured with high-angular resolution. *Investigative Ophthalmology & Visual Science*, *53*(7), pp.3405-3413.

Katz, M. and Kruger, P.B., 2013. Chapter 33: The human eye as an optical system. *Duane's Clinical Ophthalmology. Philadelphia, PA: Lippincott, Williams & Wilkins*.

Keeler, R., 2017. Allvar Gullstrand: dioptrics of the eye and the slit lamp. In *Foundations of Ophthalmology* (pp. 129-143). Springer, Cham.

Kooijman, A.C., 1983. Light distribution on the retina of a wide-angle theoretical eye. *JOSA*, *73*(11), pp.1544-1550.

LaRocca, F., Nankivil, D., Farsiu, S. and Izatt, J.A., 2013. Handheld simultaneous scanning laser ophthalmoscopy and optical coherence tomography system. *Biomedical optics express*, *4*(11), pp.2307-2321.

Le Grand, Y. and El Hage, S.G., 1980. Optics of the eye. *Physiological Optics*, pp.57-69.

LeGrand, Y. and El Hage, S.G., 2013. *Physiological optics* (Vol. 13). Springer.

Lindlein, N. and Leuchs, G., 2012. Geometrical optics. In *Springer Handbook of Lasers and Optics* (pp. 35-87). Springer, Berlin, Heidelberg.

Liou, H.L. and Brennan, N.A., 1997. Anatomically accurate, finite model eye for optical modeling. *JOSA A*, *14*(8), pp.1684-1695.

Navarro, R., Santamaria, J. and Bescós, J., 1985. Accommodation-dependent model of the human eye with aspherics. *JOSA A*, *2*(8), pp.1273-1280.

Navarro, R., González, L. and Hernández-Matamoros, J.L., 2006. On the prediction of optical aberrations by personalized eye models. *Optometry and Vision Science*, *83*(6), pp.371-381.

Navarro, R., Palos, F. and González, L., 2007. Adaptive model of the gradient index of the human lens. I. Formulation and model of aging ex vivo lenses. *JOSA A*, *24*(8), pp.2175-2185.

Goodman, J.W. and Sutton, P., 1996. Introduction to Fourier optics. *Quantum and Semiclassical Optics-Journal of the European Optical Society Part B*, *8*(5), p.1095.

Parker, A.R., 2011. On the origin of optics. *Optics & Laser Technology*, *43*(2), pp.323-329.

Pedrotti, F.L., Pedrotti, L.M. and Pedrotti, L.S., 2017. *Introduction to optics*. Cambridge University Press.

Polans, J., Jaeken, B., McNabb, R.P., Artal, P. and Izatt, J.A., 2015. Wide-field optical model of the human eye with asymmetrically tilted and decentered lens that reproduces measured ocular aberrations. *Optica*, *2*(2), pp.124-134.

Rosales, P. and Marcos, S., 2007. Customized computer models of eyes with intraocular lenses. *Optics Express*, *15*(5), pp.2204-2218.

Sen, M. and Honavar, S.G., 2021. Allvar Gullstrand: Prize and Prejudice. *Indian Journal of Ophthalmology*, *69*(6), p.1366.

Siedlecki, D., Kasprzak, H. and Pierscionek, B.K., 2004. Schematic eye with a gradient-index lens and aspheric surfaces. *Optics letters*, *29*(11), pp.1197-1199.

Smith, W.J., 2008. *Modern optical engineering: the design of optical systems*. McGraw-Hill Education.

Smith, G., Pierscionek, B.K. and Atchison, D.A., 1991. The optical modelling of the human lens. *Ophthalmic and Physiological Optics*, *11*(4), pp.359-369.

Smith, G., 1995. Invited Review Schematic eyes: history, description and applications. *clinical and experimental optometry*, *78*(5), pp.176-189.

Stenstrom, S. and Woolf, D., 1948. INVESTIGATION OF THE VARIATION AND THE CORRELATION OF THE OPTICAL ELEMENTS OF HUMAN EYES† §. *Optometry and Vision Science*, *25*(5), pp.218-232.

Tabernero, J., Benito, A., Alcón, E. and Artal, P., 2007. Mechanism of compensation of aberrations in the human eye. *JOSA A*, *24*(10), pp.3274-3283.

Tasman, W. and Jaeger, E.A. eds., 2005. *Duane's clinical ophthalmology on CD-ROM*. Lippincott Williams & Wilkins.

Thibos, L.N., Ye, M., Zhang, X. and Bradley, A., 1992. The chromatic eye: a new reduced-eye model of ocular chromatic aberration in humans. *Applied optics*, *31*(19), pp.3594-3600.

Williams, D.R., Artal, P., Navarro, R., McMahon, M.J. and Brainard, D.H., 1996. Off-axis optical quality and retinal sampling in the human eye. *Vision research*, *36*(8), pp.1103-1114.